



a package for modelling scattering-type scanning near-field optical microscopy

Tom Vincent ^{1,2}, Xinyun Liu ¹, Daniel Johnson ^{1,2}, Lars Mester ³, Nathaniel Huang ²,
Olga Kazakova ^{2,1}, Rainer Hillenbrand ^{4,5}, and Jessica Louise Boland ^{1,2}

¹Photon Science Institute, Department of Electrical and Electronic Engineering,
University of Manchester, Manchester, M13 9PL, UK

²National Physical Laboratory, Hampton Road, Teddington, TW11 0LW, UK

³Attocube Systems AG, Eglfinger Weg 2, 85540, Munich-Haar, Germany

⁴CIC NanoGUNE BRTA and Department of Electricity and Electronics, Tolosa Hiribidea,
Donostia-San Sebastián 20018, Spain

⁵IKERBASQUE, Basque Foundation for Science, Bilbao 48011, Spain

[Documentation](#)

[Code repository](#)

Scattering-type scanning near-field optical microscopy (s-SNOM) is a powerful technique for extreme subwavelength imaging and spectroscopy, with ~ 20 nm spatial resolution. But quantitative relationships between experiment and material properties requires modelling, which can be computationally and conceptually challenging. In this work, we present snompy an open-source Python library which contains implementations of two of the most common s-SNOM models, the finite dipole model (FDM) and the point dipole model (PDM). We show a series of typical uses for this package with demonstrations including simulating nano-Fourier transform infrared (FTIR) spectra and recovering permittivity from experimental s-SNOM data. We also discuss the challenges faced with this sort of modelling, such as competing descriptions of the models in literature, and finite size effects. We hope that snompy will make quantitative s-SNOM modelling more accessible to the wider research community, which will further empower the use of s-SNOM for investigating nanoscale material properties.

1 Introduction

Scattering-type scanning near-field optical microscopy (s-SNOM) is a well-established technique for probing optical properties of materials at length scales far smaller than the diffraction limit. It spans a wide spectrum across the visible^{3,4}, near-infrared (IR)⁵, mid-IR^{2,6-13}, and THz¹⁴⁻¹⁶ regions, and has applications ranging from chemical nanoidentification^{2,8}, to 2D^{3,5-7,10,12,15} and topological^{14,16} materials, to plasmonics and metamaterials^{4,6,10-12,15}, to the biological sciences^{8,9}.

But, despite its prevalence, interpretation of s-SNOM data remains challenging and requires modelling of the electromagnetic interaction between the sample and an atomic force microscopy (AFM) tip under illumination. Various models, such as the PDM¹⁷, FDM^{2,18-20}, and lightning rod model (LRM)²¹, have been proposed, which show varying levels of quantitative agreement with experimental results. However these models can be difficult to understand, and tricky to implement with computational efficiency.

To address this issue, we have created *snompy*, an open-source Python package that provides implementations of the FDM and PDM, as well as a set of related tools for modelling s-SNOM data. Figure 1 demonstrates some of the main use cases and functionalities of *snompy*, which we list below.

A crucial feature is the ability to simulate lock-in amplifier measurements of s-SNOM signals via modulation and demodulation at arbitrary harmonics, n , of an AFM tip's oscillation, as shown by the approach curves in figure 1(a).

A typical use of *snompy*, as demonstrated in figure 1(b) is to simulate nano-FTIR spectra from user-input dielectric permittivities, ϵ , which vary according to wavenumber, ν . In this example, the changing third-harmonic s-SNOM amplitude spectra from a set of hypothetical semiconducting materials with varying plasma frequency, ν_p , are simulated. The permittivities are modelled using a Drude function as detailed in section 4.6.1.

We have also introduced a new way to evaluate quasistatic reflection coefficients from layered

structures using an adapted form of the transfer matrix method (TMM), describe in section 4.4, which enables simulations of s-SNOM measurements from samples with an arbitrary number of layers. This is shown by the simulated nano-FTIR spectra from several multilayer samples featuring PMMA, PS and Si, shown in figure 1(c).

S-SNOM modelling can be computationally intensive, particularly for multilayer samples, as it relies on evaluating both definite and semi-definite integrals^{2,19,20}. We address this challenge in *snompy* by using Gauss-Laguerre quadrature to convert semi-definite integrals to finite sums, as described in section 4.5. This allows us to improve efficiency by taking advantage of NumPy-style, vectorized array broadcasting¹. It also eliminates the need to import third-party quadrature routines, meaning *snompy*'s only dependencies are Python and NumPy.

Figure 1(d) is an example simulation that takes advantage of these optimizations. It shows a series of simulated nano-FTIR spectra from PMMA on Si with three independent variables: PMMA thickness, t_{PMMA} ; wavenumber, ν ; and demodulation order, n . The 183 906 resulting points shown were calculated using vectorized array operations with no need for high-level Python loops.

Although s-SNOM is a near-field technique, far-field (Fresnel) reflection coefficients are an important part of s-SNOM modelling, as discussed in section 1.1. As such, *snompy* features an implementation of the far-field TMM, which can calculate Fresnel reflection coefficients from structures with an arbitrary number of layers. This functionality can be used in isolation from the FDM and PDM, for example to simulate polariton dispersion in polariton interferometry experiments^{3,5,6,10,16}. To demonstrate this, figure 1(e) shows a simulation of the plasmonic dispersion of a layer of graphene on Si. The permittivity model used for graphene is detailed in section 4.6.3.

In the rest of this paper, we will describe the theoretical background needed to understand s-SNOM modelling in section 1.1. We will then the FDM and PDM as they are implemented in *snompy* in sec-

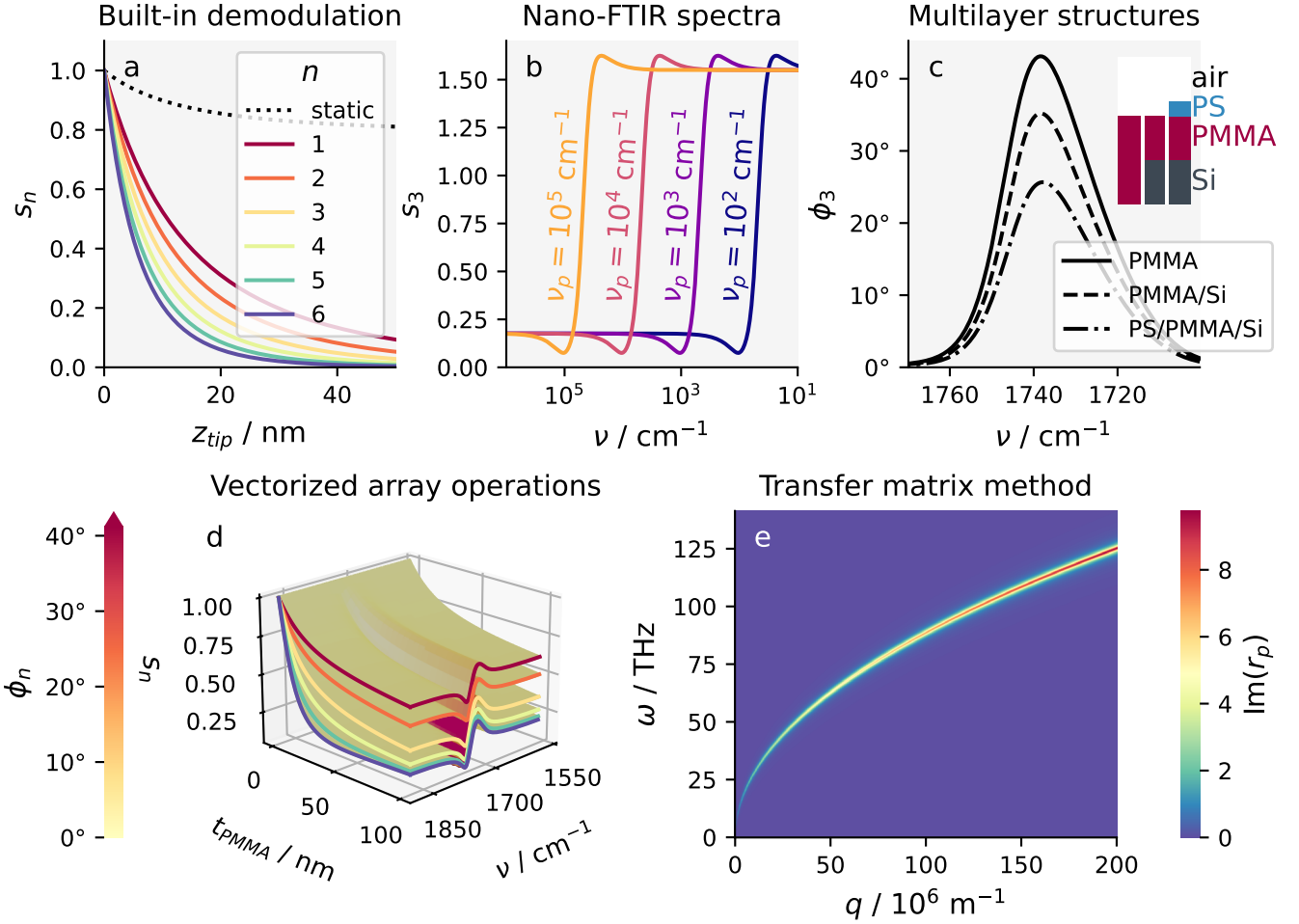


Figure 1: Showcase of snompy capabilities. **(a)** Modulation and demodulation at harmonics, n , of an atomic force microscopy (AFM) tip's oscillation. This example uses the point dipole model (PDM) to simulate the normalized decay of the s-SNOM amplitude, s_n , with tip-sample separation, z_{tip} , for the static case and for several demodulation orders. **(b)** Nano-FTIR spectra. This example uses the finite dipole model (FDM) to simulate third-harmonic amplitude spectra as a function of wavenumber, ν , from hypothetical semiconducting materials with varying plasma frequency, ν_p . **(c)** Multilayer samples. This example uses the multilayer finite dipole model (FDM) to simulate third-harmonic phase spectra from bulk PMMA, 60 nm PMMA/Si, and 20 nm PS/60 nm PMMA/Si. **(d)** Vectorized operations using NumPy-style broadcasting¹. This example uses the multilayer finite dipole model (FDM) to simulate s-SNOM spectra from PMMA/Si for a range of PMMA thicknesses, and demodulation harmonics. All 183 906 points shown were calculated simultaneously with no Python loops. The edges of the 3d surfaces for each harmonic are coloured to match (a). **(e)** Transfer matrix method (TMM) for simulating far-field (Fresnel) reflection coefficients. This example shows plasmonic dispersion for a sample of graphene on Si via the imaginary part of the in-plane wavevector-, q -, dependent Fresnel reflection coefficient, r_p . The permittivity values used for Si and PS² are $\epsilon_{Si} = 11.7$ and $\epsilon_{PS} = 2.5$. The permittivity model used for the hypothetical semiconductors is detailed in section 4.6.1. The permittivity model used for PMMA is shown in figure 4(c) and detailed in section 4.6.2. The permittivity model used for graphene is detailed in section 4.6.3. All s_n and ϕ_n values are normalized to a bulk Si reference. The specific parameters used for (a-d) are also summarized in table 4.

tions 1.2 and 1.3. Section 2 shows several demonstrations and discussions of key uses for snompy: simulating thin-film nano-FTIR spectra in section 2.1, the quantitative effects of varying model and model parameters in section 2.2, and recovering permittivity from s-SNOM data in section 4.3.

The final part of this paper, section 4 describes some of the important implementation details of snompy, as well as details of the permittivity models are used in this paper. For a comprehensive look at the details of snompy, along with tutorials and example scripts, we point users to the [online documentation](#).

1.1 Background

At the heart of the modelling approach taken by snompy is the fundamental equation governing the near-field interaction in scattering s-SNOM¹⁸:

$$\sigma \equiv \frac{E_s}{E_{in}} = (1 + r_p)^2 \alpha_{\text{eff}} \quad (1)$$

Here σ is the scattering coefficient, which is the signal of interest, and is defined as the ratio of the incident and tip-scattered light's electric fields, E_{in} and E_s . The quantity r_p is the far-field Fresnel reflection coefficient.

The other terms of this equation can be understood by referring to figure 2, which shows a typical scattering s-SNOM experiment. A focused light beam with incident electric field E_{in} shines onto an AFM tip and sample, which induces an instantaneous near-field charge polarization between the tip's apex and sample's surface, whose magnitude is governed by the tip-sample effective polarizability, α_{eff} . This polarization scatters light back into the far field with electric field E_s , meaning $\sigma \propto \alpha_{\text{eff}}$, which shows that α_{eff} contains the information about the near-field part of the s-SNOM signal.

The efficiency of scattering is enhanced by the elongated probe of the typically metal-coated AFM tip acting as an antenna, via the lightning-rod effect¹⁷.

Calculating α_{eff} requires modelling of the nanoscale light-matter interactions between the

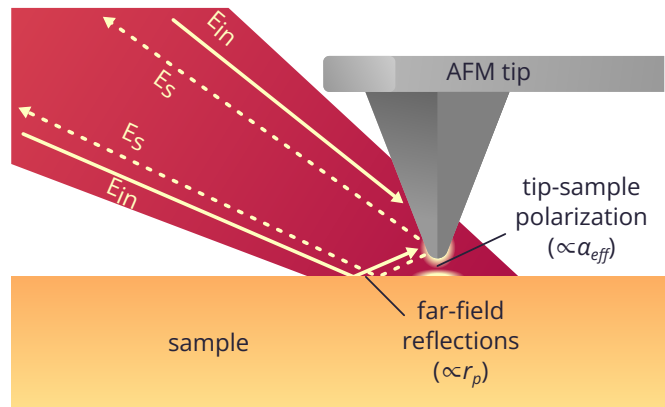


Figure 2: Diagram showing how an illuminated AFM tip scatters near-field-confined light back into the far field.

AFM tip and sample. It is strongly governed by the sample's electric permittivity ϵ (and thickness in the case of layered samples), or equivalently the quasistatic reflection coefficient of the sample's surface β . In snompy, effective polarizability can be calculated via the FDM or PDM, as described in sections 1.2 and 1.3.

The AFM tip is illuminated both directly, and indirectly by reflection from the sample surface with reflection coefficient r_p (for p-polarized light). Similarly, the scattered light from the tip is also detected directly, and indirectly after reflection from the surface. This is accounted for by the far-field reflection term $(1+r_p)^2$, which doesn't contain near-field information, but still modifies the detected s-SNOM signal.* Snompy features an implementation of the TMM²² for calculating far-field (Fresnel) reflection coefficients, which is described in section 4.4.

In experiments, the amplitude of the background scattering from the far-field light spot is many orders of magnitude greater than the amplitude of the near-field-scattered light. So scattering s-SNOM experiments typically operate the AFM in tapping mode, then use a lock-in amplifier to demodulate the detected signal at high harmonics,

*This factor is occasionally written as $(1 + cr_p)^2$, where c is an empirical weighting factor that represents the finite proportion of reflected light that takes part in the interaction^{13,23}.

n , of the tapping frequency. The detected signal is then given, not by equation 1 but by¹⁷:

$$\sigma_n = (1 + r_p)^2 \alpha_{\text{eff},n} \quad (2)$$

Here, and throughout this paper, a subscript n refers to quantities which are demodulated at the n^{th} harmonic of the AFM tapping frequency. For details of how these quantities are calculated, see section 4.2.

A final nuance that needs to be accounted for is that the measured σ_n signal depends on instrumental factors, such as the detector sensitivity and E_{in} , which are usually unknown. For quantitative results, it is therefore necessary to normalize the measured values to measurements taken from a reference sample with a well-known dielectric function. Au and Si are common choices as they are spectrally flat in the mid-IR.

The normalized signal, often called the near-field contrast^{13,18}, is therefore given by:

$$\eta_n = \frac{\sigma_n}{\sigma_n^{(\text{ref})}} = \frac{(1 + r_p)^2}{(1 + r_p^{(\text{ref})})^2} \left(\frac{\alpha_{\text{eff},n}}{\alpha_{\text{eff},n}^{(\text{ref})}} \right) \quad (3)$$

Here a superscript (ref) refers to parameters taken from the reference sample used for normalization.

The parameter η_n is a complex number that represents both the amplitude, s_n , and phase, ϕ_n , of the near-field scattered light as:

$$\begin{aligned} \eta_n &= s_n e^{i\phi_n} \\ s_n &= |\eta_n| \\ \phi_n &= \arg(\eta_n) \end{aligned} \quad (4)$$

1.2 Finite dipole model

The FDM was initially derived for bulk samples by Cvitkovic *et al.* (2007)¹⁸, then extended to multi-layer samples by Hauer *et al.* (2012)¹⁹. A slightly modified implementation was also presented by Mester *et al.* (2020)².

These are the versions included in *snumpy*, and thus described below, however we stress that

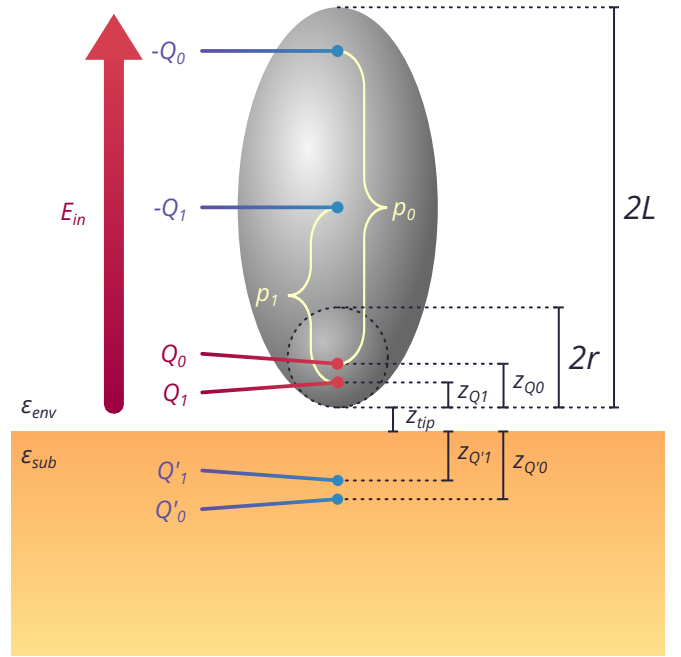


Figure 3: Image showing an ellipsoid model of an AFM tip over a semi-infinite sample, along with the model charges and image charges used to derive the bulk FDM.

there are several other FDM implementations described in literature²⁴⁻²⁶.

1.2.1 Bulk samples

The FDM models an AFM tip as a perfectly conducting ellipsoid, with radius of curvature r_{tip} and semi-major axis length L_{tip} , as shown in figure 3. By making the quasistatic approximation, we can model the response of the tip to far-field light by the response to a vertically oriented static electric field of strength E_{in} .

In the absence of a sample, the field around the ellipsoid can be approximated by a dipole formed of two charges $\pm Q_0$ at distances z_{Q_0} from the ends of the ellipsoid²⁷, where:

$$z_{Q_0} \approx \frac{1.31 L_{tip} r_{tip}}{L_{tip} + 2r_{tip}} \quad (5)$$

The strength of this dipole is given by:

$$\begin{aligned} p_0 &= 2(L_{tip} - z_{Q_0})Q_0 \\ &\approx 2L_{tip}Q_0, \quad \text{for } r_{tip} \ll L_{tip} \end{aligned} \quad (6)$$

When the tip is brought close to a sample surface, we make the assumption that only the charge Q_0 interacts with the sample, due to the large distance from the $-Q_0$ charge. The tip-sample interaction can then be modelled using the method of image charges.

The response of the sample to Q_0 can be modelled with an image charge Q'_0 below the interface. For bulk samples, the value of this charge is determined by the quasistatic reflection coefficient, β , as:

$$Q'_0 = \beta Q_0 \quad (7)$$

The value of β can be found from the environment and substrate permittivities ϵ_{env} and ϵ_{sub} as:

$$\beta = \frac{\epsilon_{env} - \epsilon_{sub}}{\epsilon_{env} + \epsilon_{sub}} \quad (8)$$

This image also asserts an influence back on the tip, which we model with an extra charge Q_1 at a

distance $z_{Q_1} = \frac{r_{tip}}{2}$ from the end of the tip. Q_1 has its own image, Q'_1 , and for charge conservation we must add a counter charge $-Q_1$ at the centre of the tip^{18,19}.

The value of Q_1 can be solved for by accounting for contributions to the overall polarization from Q_0 , and also from Q_1 itself, as:

$$Q_1 = \beta(f_0^{(B)}Q_0 + f_1^{(B)}Q_1) \quad (9)$$

Here the $f_j^{(B)}$ values are functions encapsulating the geometry of the system*, given by:

$$f_j^{(B)} = \left(g - \frac{r_{tip} + 2z_{tip} + z_{Q_j}}{2L_{tip}} \right) \frac{\ln \left(\frac{4L_{tip}}{r_{tip} + 4z_{tip} + 2z_{Q_j}} \right)}{\ln \left(\frac{4L_{tip}}{r_{tip}} \right)} \quad (10)$$

The factor g here is a dimensionless weighting factor that modifies the proportion of the total charge that takes part in the interaction, this is typically set to $g = 0.7e^{0.06i}$.

The charges Q_1 and $-Q_1$ form another dipole:

$$\begin{aligned} p_1 &= (L_{tip} - z_{Q_1})Q_1 \\ &\approx L_{tip}Q_1, \quad \text{for } r_{tip} \ll L_{tip} \end{aligned} \quad (11)$$

The effective polarizability can then be found from the total induced dipole, as:

$$\begin{aligned} \alpha_{eff} &= \frac{p_0 + p_1}{E_{in}} \\ &\approx 2L_{tip} \frac{Q_0}{E_{in}} \left(1 + \frac{f_0^{(B)}\beta}{2(1 - f_1^{(B)}\beta)} \right) \end{aligned} \quad (12)$$

The constant of proportionality here can be neglected as it depends on the unquantified $\frac{Q_0}{E_{in}}$ ratio, leading to the final result:

$$\alpha_{eff} \propto 1 + \frac{f_0^{(B)}\beta}{2(1 - f_1^{(B)}\beta)} \quad (13)$$

*We use the superscript (B) to distinguish these bulk geometry functions $f^{(B)}$ from their multilayer equivalents $f^{(M)}$ used in the multilayer implementation of the FDM (see section 1.2.2).

1.2.2 Multilayer samples

Hauer *et al.* proposed a method to extend the FDM to multilayer samples¹⁹. In this method, the response of the multilayer sample to a charge Q_j is modelled with a single image charge $Q'_j = \beta_{Q'_j} Q_j$ at a depth $d_{Q'_j}$ below the sample surface.

The effective depth and reflection coefficient for the charge are chosen to be those that preserve the normal electric field E_z and potential ϕ at the surface of the sample, as:

$$\begin{aligned} d_{Q'_j} &= \left| \frac{\phi|_{z=0}}{E_z|_{z=0}} \right| - z_{Q_j}, \quad \text{and} \\ \beta_{Q'_j} &= \frac{(\phi|_{z=0})^2}{E_z|_{z=0}} \end{aligned} \quad (14)$$

The potential and field can be calculated from:

$$\begin{aligned} \phi|_{z=0} &= \int_0^\infty \beta^{(M)}(q) e^{-2z_{Q_j} q} dq, \quad \text{and} \\ E_z|_{z=0} &= \int_0^\infty \beta^{(M)}(q) q e^{-2z_{Q_j} q} dq \end{aligned} \quad (15)$$

Here q is the in-plane momentum of light, and $\beta^{(M)}$ is the effective quasistatic reflection coefficient for the surface (see section 4.4 for details of how this is calculated in snompy).

These values can then be inserted into a modified version of equation 13, as:

$$\alpha_{\text{eff}} \propto 1 + \frac{f_0^{(M)} \beta_{Q'_0}}{2 \left(1 - f_1^{(M)} \beta_{Q'_1} \right)} \quad (16)$$

The geometry function is also modified in this case to become:

$$f_j^{(M)} = \left(g - \frac{r_{\text{tip}} + z_{\text{tip}} + d_{Q'_j}}{2L_{\text{tip}}} \right) \frac{\ln \left(\frac{4L_{\text{tip}}}{r_{\text{tip}} + 2z_{\text{tip}} + 2d_{Q'_j}} \right)}{\ln \left(\frac{4L_{\text{tip}}}{r_{\text{tip}}} \right)} \quad (17)$$

1.2.3 Charge average method

Mester *et al.* proposed another multilayer FDM method², which is also included in snompy.

In this implementation, the geometry function used is $f^{(B)}$, the same as for the bulk FDM method, however an alternative expression for the quasistatic reflection coefficient is used, which is derived from the ratio of the fields at the height of the probe:

$$\bar{\beta} = \frac{\int_0^\infty \beta^{(M)}(q) q e^{-2z_{Q_a} q} dq}{\int_0^\infty q e^{-2z_{Q_a} q} dq} \quad (18)$$

The height z_{Q_a} here is the height of a single representative test charge Q_a , whose position within the tip is chosen empirically. A value of $z_{Q_a} = z_{\text{tip}} + 1.4r_{\text{tip}}$ was found to produce the best agreement with experimental s-SNOM spectra in the original reference².

This can then be inserted into another modified version of equation 13, as:

$$\alpha_{\text{eff}} \propto 1 + \frac{f_0^{(B)} \bar{\beta}}{2 \left(1 - f_1^{(B)} \bar{\beta} \right)} \quad (19)$$

1.3 Point dipole model

The PDM is an older alternative to the FDM which typically has less quantitative agreement with experiment^{18,19}. However, it has some advantages in that it is conceptually simpler and can account for the dielectric function of the AFM tip, so it is also featured in snompy.

In the PDM, the tip is first modelled as a dielectric sphere whose response to electric fields is then represented by a single point dipole, located in the sphere's centre^{17,18}. The effective polarizability is given by:

$$\alpha_{\text{eff}} = \frac{\alpha_{\text{tip}}}{1 - f^{(P)} \beta} \quad (20)$$

Here α_{tip} represents the polarizability of the model sphere, which relates to the tip permittivity ϵ_{tip} and radius r_{tip} as:

$$\alpha_{tip} = 4\pi r_{tip}^3 \frac{\epsilon_{tip} - 1}{\epsilon_{tip} + 2} \quad (21)$$

The function $f^{(P)}$ encapsulates extra geometric properties of the system and is given by:

$$f^{(P)} = \frac{\alpha_{tip}}{16\pi (r_{tip} + z_{tip})^3} \quad (22)$$

2 Results

2.1 Thin-film nano-FTIR spectra

In this section we will demonstrate a typical use of snompy by using the FDM to simulate nano-FTIR spectra from different thicknesses of PMMA on a Si substrate, normalized against a bulk Si reference, and to compare them with experimental data reproduced with permission from Mester *et al.*²

Figures 4(a) and (b) show simulated and experimental third-harmonic amplitude, s_3 , and phase, ϕ_3 , spectra from PMMA samples ranging from 9 to 100 nm in thickness.

To simulate a s-SNOM signal using the FDM, we need to input various parameters which describe the effective shape and properties of the AFM tip. For this simulation we used the parameters reported in the original work by Mester *et al.*, and these parameters are reported in table 4. The effects of various parameters of the FDM are discussed in section 2.2.

We also need to input dielectric permittivities for all of the constituent materials. In the mid-IR, the permittivity of Si is given by $\epsilon_{Si} = 11.7$ ². We represent the permittivity of PMMA, ϵ_{PMMA} , by a broadened Lorentzian oscillator at the frequency of its C=O bond. This is shown in figure 4(c). The specific parameters for ϵ_{PMMA} were chosen to best reproduce the experimental data, and are given in section 4.6.2.

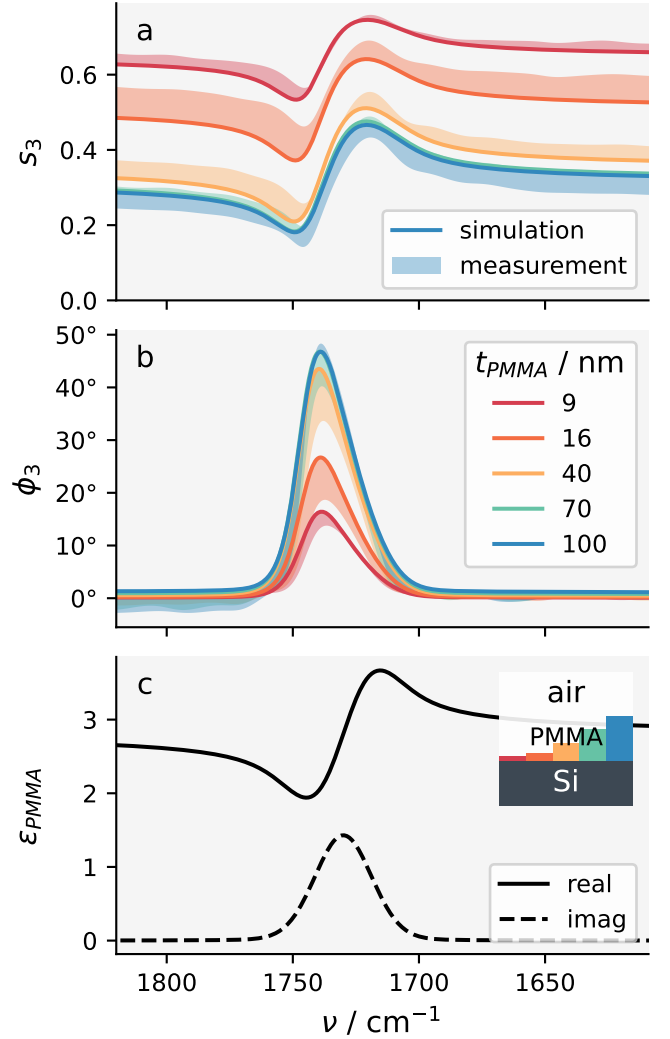


Figure 4: Simulated and experimental nano-FTIR spectra from samples with varying thicknesses of PMMA on Si. **(a)** The third-harmonic s-SNOM amplitude. **(b)** The third-harmonic s-SNOM phase. **(c)** The simulated dielectric function of PMMA, chosen to best reproduce the experimental data (inset: schematic of sample layer structure). Filled curves in (a) and (b) show the differences between the experimental and simulated data. The experimental data is reproduced with permission from Mester *et al.*². All signals shown are normalized to a bulk Si reference with $\epsilon_{Si} = 11.7$. The specific parameters used for each plot are also summarized in table 4.

Note that the resulting permittivity shown is slightly higher than previous measurements acquired by ellipsometry from bulk samples². This could potentially arise from sample differences, such as different proportions of cross-linking between bulk and thin-film samples.

However the permittivity we show is qualitatively similar to previous measurements, and leads to a good agreement between simulation and experiment, so we conclude that it is a reasonable model for the PMMA in these measurements.

2.2 Effects of varying model and parameters

For quantitative comparisons between modelling and experiments, it is important to choose model parameters reproduce the measured results well. A common way to calibrate the model parameters is to fit them to experimental approach curves^{18,19,28}, in which the signal is measured as a function of tip-sample separation, z_{tip} .

As described in section 1.2, the FDM represents an AFM tip as a perfectly conducting ellipsoid with tapping amplitude A_{tip} , apex radius of curvature r_{tip} , and semi-major axis length L_{tip} . In this section we use the FDM to investigate the effects of varying these parameters on a series of approach curves taken from Si, with permittivity $\epsilon_{Si} = 11.7$, and a series of spectra taken from a sample of 60 nm of PMMA on Si, where the modelled permittivity of PMMA is the same as shown in figure 4(c).

Figures 5(a) and (b) show the effect of varying the tapping amplitude. The approach curves reveal that a lower tapping amplitude leads to a faster decay of the s-SNOM signal with distance from the sample, z_{tip} . This is because a reduced tapping amplitude leads to a reduced interaction volume, which consequently increases the surface sensitivity of the measurement¹⁴, meaning tapping amplitude can be an effective way to adjust the degree of near-field confinement.

Figure 5(b) demonstrates that tapping amplitude also has an effect on the lineshape and apparent

frequency of resonances in nano-FTIR spectra. This shows that correctly calibrated measurements of tapping amplitude are important for quantitative s-SNOM modelling.

Figures 5(c) to (f) show the effects of varying the effective radius and length of the model ellipsoid. Unlike tapping amplitude, which is typically a controlled parameter in s-SNOM experiments, these may be unknown values which require fitting to best reproduce the experimental data.

The spectra reveal that both tip radius and length have an effect on the amplitude and apparent frequency of resonances in nano-FTIR spectra, however in opposite directions. Comparatively, the approach curves demonstrate that the radius has a more significant effect on the decay of the near-field signal.

As well as the effects of varying parameters within a particular model, it is also important to consider the effects of changing the model itself. Figure 6 highlights the quantitative differences between simulations using the PDM and FDM with similar parameters, and also between the multilayer model as described by Hauer *et al.* (see section 1.2.2) and the charge average method (see section 1.2.3).

The results in this section highlight the importance of well-chosen model and model parameters for quantitative agreement with experiment. As such, it is important that any modelling tool allows full and flexible control over the constituent parameters of the models it implements. Section 4.1 details the main functions included in *snumpy* and gives descriptions of all controllable parameters.

2.3 Recovering material properties

The typical use case for the FDM, as demonstrated above, is to simulate s-SNOM measurements from user-input model samples. Comparatively few works have focused on using the FDM to recover sample properties from experimental s-SNOM measurements^{14,24,25,28}, though this is also an attractive use case.

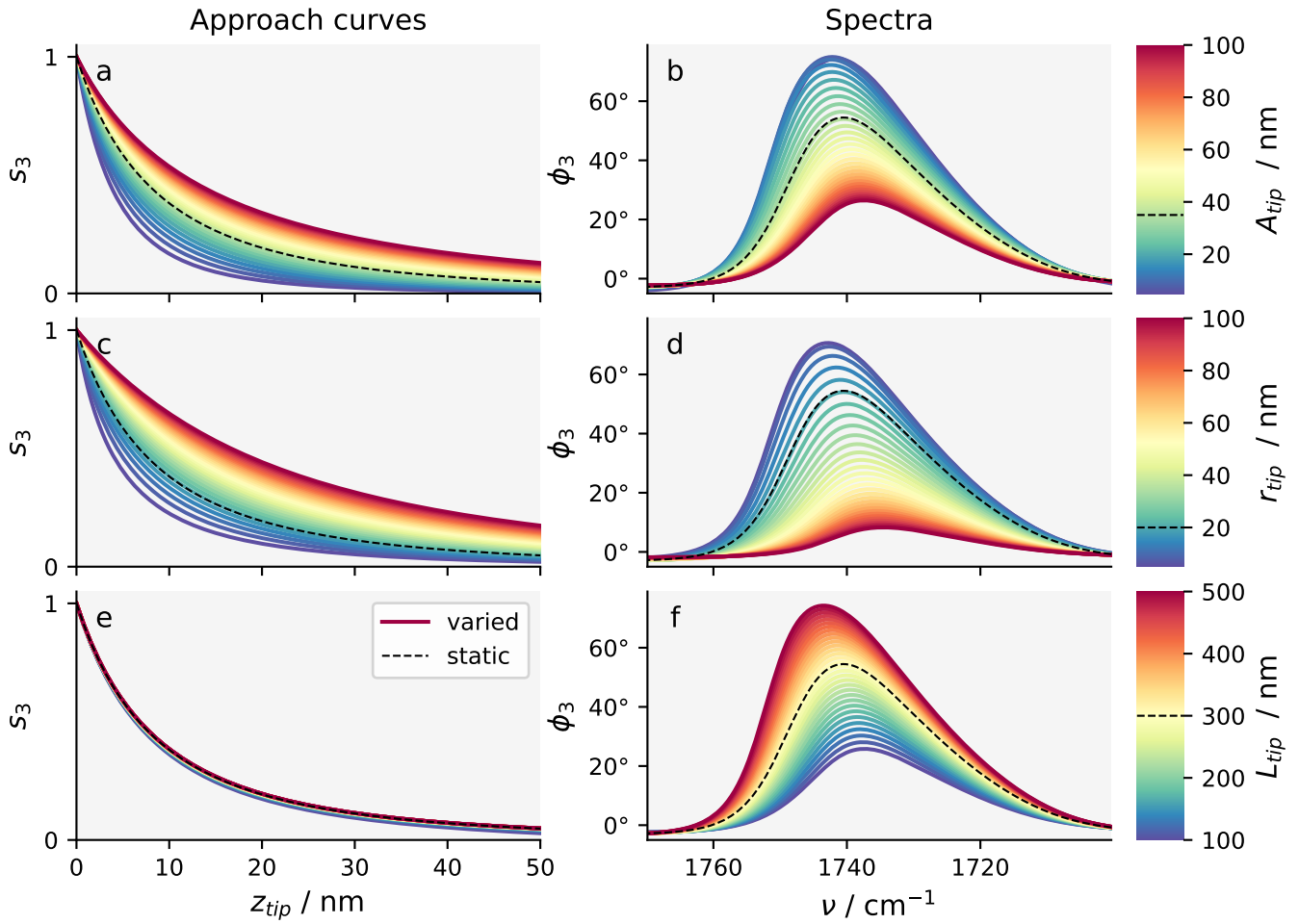


Figure 5: Effects of varying model parameters. FDM-simulated approach curves from a bulk Si sample and spectra from a sample of 60 nm of PMMA on Si with varying: **(a, b)** tapping amplitude, A_{tip} ; **(c, d)** tip radius, r_{tip} ; and **(e, f)** tip semi-major axis length, L_{tip} . Black dashed lines on colour scales represent the fixed value of the corresponding quantity used in the other plots of this figure. The dielectric permittivity model used for PMMA is shown in figure 4(c). All signals shown are normalized to a bulk Si reference with $\epsilon_{Si} = 11.7$. The specific parameters used for each plot are also summarized in table 4.

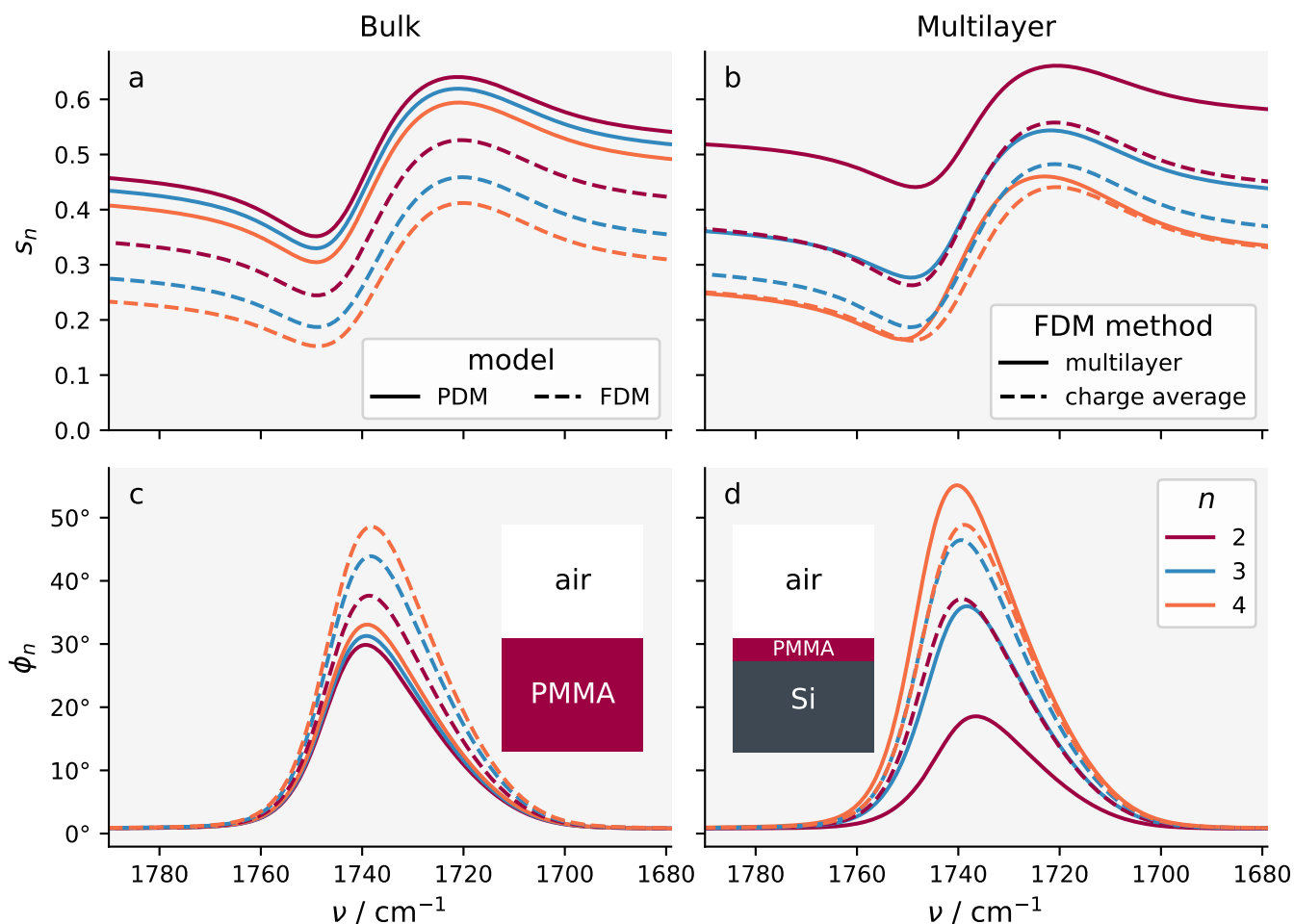


Figure 6: Quantitative differences between different s-SNOM models. The spectra on the left compare the point dipole model (PDM) and finite dipole model (FDM) for a sample of bulk PMMA, and the spectra on the right compare two different multilayer FDM implementations for a sample of 60 nm PMMA on bulk Si. Panels show: **(a, b)** amplitude spectra, s_n ; and **(c, d)** phase spectra, ϕ_n , for three demodulation harmonics, n . Insets in (c) and (d) show schematics of the simulated materials. The dielectric permittivity model used for PMMA is shown in figure 4(c). All signals shown are normalized to a bulk Si reference with $\epsilon_{\text{Si}} = 11.7$. The specific parameters used for each plot are also summarized in table 4.

In this section we will discuss some different approaches to tackle this problem, as well as some typical challenges encountered in the process.

Sample properties in the FDM can be represented via their permittivity ϵ . The primary challenge in inverting the FDM, is that the expression for the s-SNOM contrast, η_n , as a function of ϵ is impossible to invert algebraically^{24,25} (see sections 1.1 and 1.2 for a description of this function).

To better visualize the problem we are trying to solve, figure 7 plots $\eta_n = s_n e^{i\phi_n}$, as a function of ϵ for four harmonics, n , normalized to a Si reference with $\epsilon_{\text{Si}} = 11.7$. This reveals the complicated variation of η_n , with some regions appearing relatively flat while others feature lots of local variation (note the log scaling of the s_n scale). The varying sensitivity of η_n to small changes in ϵ can make recovering ϵ challenging, particularly in the presence of experimental noise, as small errors in η_n can lead to relatively large errors in the corresponding ϵ value.

One approach to recovering ϵ that has had some success in literature^{14,28}, is to use minimization routines to minimize the difference between the observed and simulated η_n . However, this approach can be computationally expensive, as it typically relies on many independent function calls.

It also suffers from the fact that η_n as a function of ϵ is a poorly conditioned function for minimization. For example, on top of the above-mentioned varying sensitivity of the function, there are also multiple values of ϵ which can produce identical values of η_n . One such pair of values is indicated as an example in figures 7(d) and (h). These indistinguishable points can potentially lead to false solutions during minimization.

The number of false solutions can be reduced by restricting the permitted ϵ values to only those with a positive imaginary part, as we have done here.

We show an example of a simulated experiment that uses minimization to attempt to recover ϵ from η in figure 8. A simulated permittivity, shown in figure 8(a), is used to generate a third-harmonic nano-FTIR spectrum, shown in figure 8(b).

SciPy's `scipy.optimize.minimize` function²⁹ is then used to find the ϵ value that minimizes the function:

$$\left| \eta_3^{((\text{test}))}(\epsilon) - \eta_3^{((\text{obs}))} \right| \quad (23)$$

Here a superscript (obs) refers to the observed value and (test) to the ϵ -dependent test value that should be adjusted to match it. The results from this are shown by the dashed lines in figure 8(c). To show the sensitivity of the recovery to noise, some simulated noise is added to the spectra in figure 8(b), shown by filled areas above and below the curves, and the results of minimizing the noisy spectra are also shown in figure 8(c).

Another successful approach^{2,24,25} is to express $\alpha_{\text{eff},n}$ as a truncated Taylor series in β , which can be related to ϵ using equation 8. The expression is then possible to invert algebraically and solutions can be found by finding the complex roots of a high-order polynomial. The derivation of the Taylor expansion for the FDM used in `snumpy` is shown in section 4.3.

A downside of this approach is that the Taylor expansion only converges for values of $|\beta| \ll 1$. This is usually only true for weak molecular oscillators, which prevents the method being used for samples with strong light-matter oscillations, such as metals and polaritonic materials.

This Taylor series method of inversion is implemented natively in `snumpy`, with no need to import external minimization routines as we did for the example above. We ran this inversion on the same simulated spectra as for the previous example and the results from this are shown by the solid lines in figure 8(c). Note that there are no solutions returned in the coloured area of the graph, where $|\beta| > 1$.

We stress that the recovery of ϵ from the simulated s-SNOM spectra in this section are an idealized case, which is free from systematic errors and in which the same model is used to both generate the data and to perform the recovery. When working with experimental data, the limitations and applicability of the model must be taken into account.

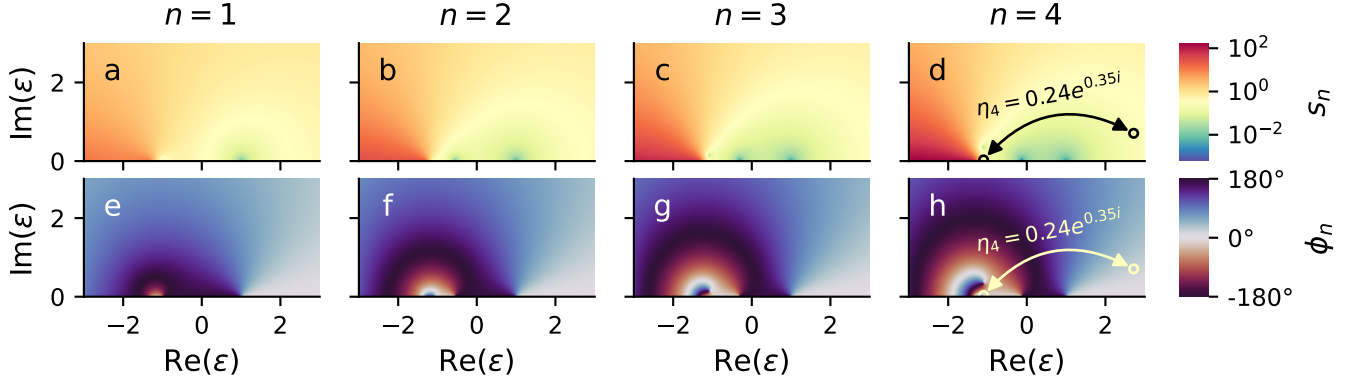


Figure 7: S-SNOM signals as a function of permittivity. Images show: **(a-d)** the amplitude, s_n ; and **(e-f)** the phase, ϕ_n ; of a s-SNOM measurement normalized to bulk Si for harmonics $n = 1$ to 4. Note the log scaling of the colour mapping in figures (a-d). Arrows and small circles in panels (d) and (h) show an example of two points with different ϵ values but indistinguishable $\eta_4 = s_4 e^{i\phi_4}$ values. The specific parameters used for this calculation are summarized in table 4.

Indeed, one final and fundamental challenge to inverting the FDM to recover material properties from experimental data, is that the model does not account for finite-size effects^{13,18}. Samples are modelled as semi-infinite planar structures, which means any effects related to factors such as reflections or standing waves cannot be reproduced. A detailed discussion of these effects is beyond the scope of this paper, but the extent to which finite size effects can be accounted for in FDM modelling could form the basis of future studies.

3 Discussion

The models we have made accessible as open-source code in *snumpy* have had considerable success in literature for producing quantitative agreement with experiments^{2,18,19}. However, there are certain challenges which must also be addressed.

One particularly common issue is that these models assume semi-infinite, planar samples, so they cannot account for effects introduced by finite lateral sample dimensions, which includes many commonly studied effects such as surface polaritons and standing waves in nanophotonic structures. This is particularly problematic, as one of the main motivators for using s-SNOM instead of far-field optical microscopy is to image structures

smaller than the diffraction limit, so finite lateral dimensions are a characteristic feature of many s-SNOM samples. Other models, which are not currently implemented in *snumpy*, such as those described by Chen *et al.*^{30,31}, have attempted to address this by accounting for laterally varying sample dimensions.

Furthermore, in the process of adapting models from their descriptions in literature, we have identified many conflicting interpretations of the FDM^{13,18,19,24-26}, which differ in terms of how they account for multilayer samples, and how they evaluate quasistatic reflection coefficients, among other details. This is a natural consequence of different groups working in parallel on complicated models.

We showed in section 2.2 that two models included in *snumpy*, the Hauer multilayer method¹⁹ and the charge average method^{2,20}, lead to quantitative differences for comparable input parameters, and we can expect that other implementations will produce similar model-to-model quantitative differences. We stress that this is not an indication that any particular model is at fault, only that the parameters needed to agree with experimental data must be chosen for the specific implementation being used. However, these discrep-

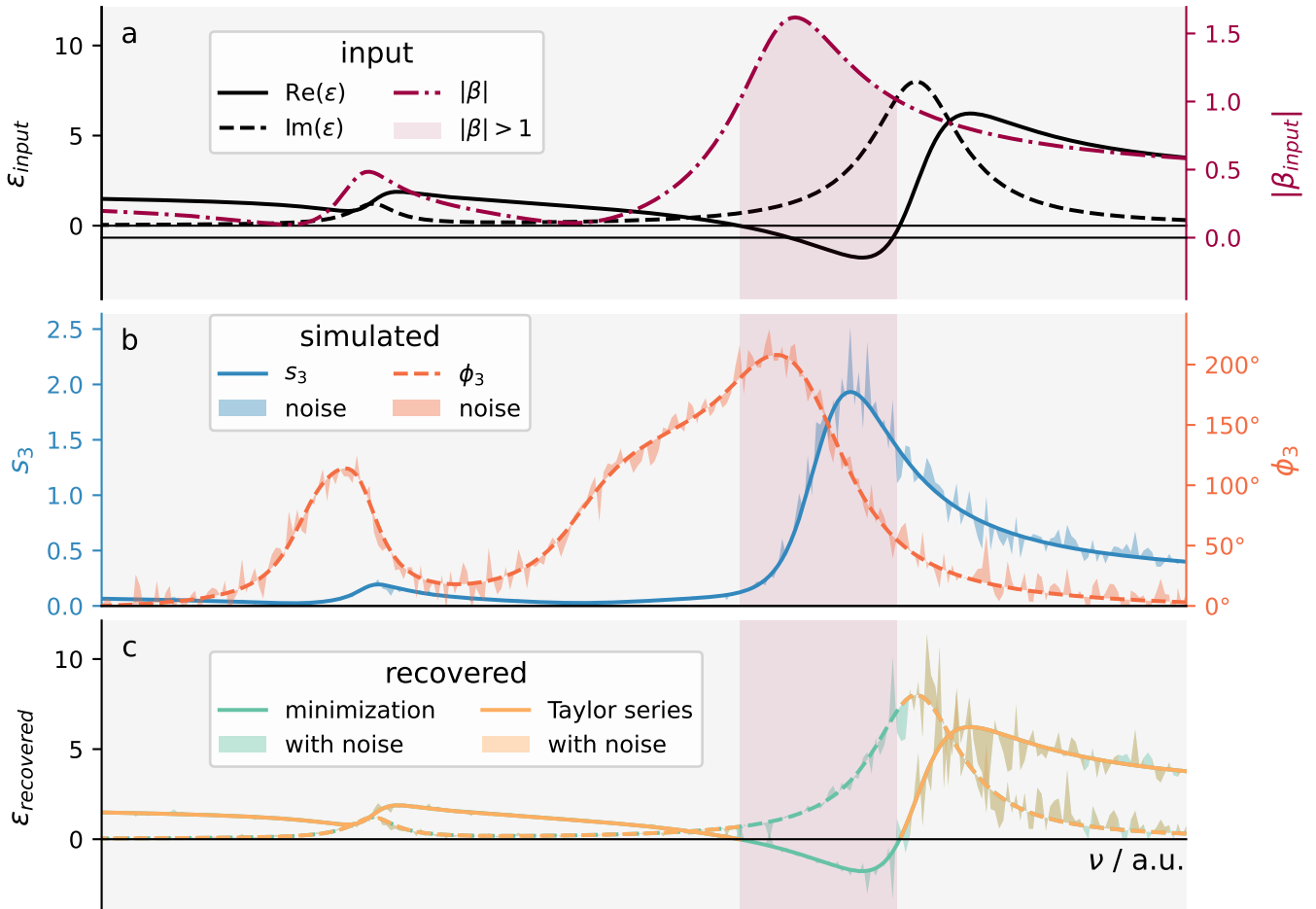


Figure 8: Recovering permittivity from s-SNOM signals. **(a)** A simulated permittivity, ϵ , and its corresponding quasistatic reflection coefficient, β , featuring both a weak oscillator ($|\beta| < 1$) and a strong oscillator ($|\beta| > 1$). The region of strong light-matter interaction with $|\beta| > 1$ is coloured in red. **(b)** Simulated third-harmonic s-SNOM signal $\eta_3 = s_3 e^{i\phi_3}$, using the FDM. Some simulated experimental noise was added, shown by filled areas above and below the lines. **(c)** Permittivity recovered from the pristine and noisy s-SNOM spectra shown in (b), using both minimization and by using the Taylor series method. Note that the Taylor series method returns no valid solutions in the region where $|\beta| > 1$. The specific parameters used for these calculations are summarized in table 4.

ancies do warrant further comparison, and this is one area where we believe open-source modelling software can be particularly beneficial.

We note that of all the FDM implementations we encountered, the description by Hauer *et al.*¹⁹ seems to be the most ubiquitous in literature, so we have chosen this as the default implementation in `snompy`.

The extent to which these challenges interfere with quantitative s-SNOM modelling must be understood before this modelling can become a widely accessible and useful tool for probing nanoscale material properties. But this will require methodical work, and comparison between models and carefully designed test samples to identify the regimes where the models are no longer applicable. By publishing `snompy`, which contains efficient and usable open-source implementations of the FDM, we hope to make this vital work faster, easier and more transparent.

A further advantage of making `snompy` open-source is that we can invite contributions from the wider research community, and take advantage of expertise beyond that of our own group and collaborators. For example, in future versions of `snompy`, we would be keen to include additional s-SNOM models, beyond the FDM and PDM which we have already implemented, such as the LRM²¹ and those models that account for varying sample geometry^{30,31}. In this way, we hope that `snompy` will be a valuable and evolving resource for the s-SNOM community for many years to come.

4 Methods

4.1 Programming interface details

In this section we give some details of the programming interface to the functions contained within `snompy`, we also give the specific parameters used for the example simulations in this paper. We stress that this section is intended as an overview, and is not a guide for users of `snompy`. For a comprehensive look at the details of `snompy`, along with tutorials and example scripts, we point

users to the [online documentation](#).

The primary methods provided by `snompy` are the expressions for effective polarizability, α_{eff} , and the n^{th} -harmonic-demoduated effective polarizability, $\alpha_{\text{eff},n}$, using the FDM and PDM, which are summarized below in table 1.

model	parameter	method
FDM	α_{eff}	<code>snompy.fdm.eff_pol()</code>
FDM	$\alpha_{\text{eff},n}$	<code>snompy.fdm.eff_pol_n()</code>
PDM	α_{eff}	<code>snompy.pdm.eff_pol()</code>
PDM	$\alpha_{\text{eff},n}$	<code>snompy.pdm.eff_pol_n()</code>

Table 1: Effective polarizability methods in `snompy`.

Of these, the `eff_pol_n()` functions are adaptations of the `eff_pol()` functions with extra arguments related to demodulation. We will list the main arguments for the two `eff_pol_n()` functions to show the degree of control possible with `snompy`. The arguments for `snompy.fdm.eff_pol_n()` are given in table 2, and the arguments for `snompy.pdm.eff_pol_n()` are given in table 3.

The first argument for both `eff_pol_n()` should be an instance of a `snompy.Sample` object. This is an object that represents a sample as a stack of dielectric layers with a semi-infinite substrate and superstrate (the environment above the sample surface). The user is able to specify the permittivity and thickness of each layer to define the s-SNOM simulation. The sample object also has methods for calculating far-field and quasistatic reflection coefficients as described in section 4.4.

The specific parameters used to calculate all η_n simulations shown in this work are summarized in table 4

argument	symbol	description
sample	—	Object representing a sample.
A_tip	A_{tip}	The tapping amplitude of the AFM tip.
n	n	The harmonic of the AFM tip tapping frequency at which to demodulate.
z_tip	z_{tip}	Height of the tip above the sample.
r_tip	r_{tip}	Radius of curvature of the AFM tip.
L_tip	L_{tip}	Semi-major axis length of the effective spheroid from the finite dipole model.
g_factor	g	Empirical weighting factor (described in section 1.2.1).
d_Q0	$\frac{z_{Q0}}{r_{tip}}$	Depth of an induced charge 0 within the tip, in units of r_{tip} .
d_Q1	$\frac{z_{Q1}}{r_{tip}}$	Depth of an induced charge 1 within the tip, in units of r_{tip} .
method	—	The method of the finite dipole model to use: "bulk", "multi" or "Q_ave".
d_Qa	$\frac{z_{Qa}}{r_{tip}}$	Depth of a test charge a within the tip, in units of r_{tip} (only used by the "Q_ave" implementation).

Table 2: Arguments for `snompy.fdm.eff_pol_n()`. The first column is the variable name in the code and the second is the mathematical symbol used in this paper.

argument	symbol	description
sample	—	Object representing a sample.
A_tip	A_{tip}	The tapping amplitude of the AFM tip.
n	n	The harmonic of the AFM tip tapping frequency at which to demodulate.
z_tip	z_{tip}	Height of the tip above the sample.
r_tip	r_{tip}	Radius of curvature of the AFM tip.
eps_tip	ϵ_{tip}	Permittivity of the tip (ignored if <code>alpha_tip</code> specified).
alpha_tip	α_{tip}	Polarizability of the conducting sphere used as a model for the AFM tip.

Table 3: Arguments for `snompy.pdm.eff_pol_n()`. The first column is the variable name in the code and the second is the mathematical symbol used in this paper.

figure	n	A_{tip} / nm	r_{tip} / nm	L_{tip} / nm	g	ϵ_{tip}	method
1(a)	1-6	30	30	—	—	∞	PDM
1(b)	3	30	30	200	0.6	—	FDM (bulk)
1(c)	3	30	30	200	0.6	—	FDM (multilayer)
1(d)	1-6	30	30	200	0.6	—	FDM (multilayer)
1(d)	1-6	30	30	200	0.6	—	FDM (multilayer)
4(a, b)	3	30	30	200	0.6	—	FDM (charge average)
5(a, c, e)*	3	35	20	300	$0.7e^{0.06i}$	—	FDM (bulk)
5(b, d, f)*	3	35	20	300	$0.7e^{0.06i}$	—	FDM (multilayer)
6(a, c)	2-4	30	30	200	0.6	∞	PDM / FDM (bulk)
5(b, c)	2-4	30	30	200	0.6	—	FDM (multilayer / charge average)
7	1-4	35	20	300	$0.7e^{0.06i}$	—	FDM (bulk)
8(b)	3	30	20	300	$0.7e^{0.06i}$	—	FDM (bulk)

Table 4: Input parameters for all η_n calculations shown in this work. All η_n , s_n and ϕ_n signals shown are normalized to a sample of bulk Si with $\epsilon_{\text{Si}} = 11.7$ acquired with the same model parameters. *Parameters for figure 5 represent the fixed values only, shown by black dashed lines in the plots.

4.2 Simulating demodulation

S-SNOM relies on lock-in amplifier demodulation of z_{tip} -dependent signals at different harmonics, n , of the AFM tip's tapping frequency.

To model this we first define a height modulation as:

$$z'_{tip}(\theta; z_{tip}, A_{tip}) = z_{tip} + A_{tip}(1 + \cos(\theta)) \quad (24)$$

Here z'_{tip} is the modulated version of z_{tip} , A_{tip} is the tapping amplitude and θ is the phase of the AFM's tapping cycle*.

To simulate demodulation at a harmonic, n , we multiply the input signal by a complex sinusoid, then integrate over one period of the tip oscillation.

*Note that the cosine term here is offset so that the bottom of the oscillation is at z_{tip} (rather than at $z_{tip} - A_{tip}$). This ensures that when the nominal value of $z_{tip} = 0$ the oscillation never becomes negative (which would mean intersecting with the sample surface).

tion.

We represent this with an operator \hat{F} to convert an arbitrary, z_{tip} -dependent function G into its modulated and demodulated equivalent G_n , as:

$$\begin{aligned} G_n(z_{tip}; A_{tip}, n) &\equiv \hat{F}[G(z_{tip}); A_{tip}, n] \\ &\equiv \frac{1}{2\pi} \int_{-\pi}^{\pi} G(z'_{tip}(\theta; z_{tip}, A_{tip})) e^{in\theta} d\theta \end{aligned} \quad (25)$$

This can be evaluated efficiently using simple quadrature methods such as the trapezium method.

4.3 Taylor series representation

For samples with weak light-matter interactions, such that the magnitude of the quasistatic reflection coefficient $|\beta| \ll 1$, β can be recovered from the demodulated effective polarizability $\alpha_{\text{eff},n}$

with the help of a Taylor series representation of $\alpha_{\text{eff},n}$ ^{2,20,24,25}. In this section we describe how this is implemented in snompy.

For the bulk FDM formula given in equation 13 we can represent the effective polarizability by a Taylor series in β as:

$$\alpha_{\text{eff}} \propto 1 + \frac{f_0^{(B)}}{2} \sum_{j=1}^{\infty} \left(f_1^{(B)}\right)^{j-1} \beta^j \quad (26)$$

Using the notation defined in section 4.2, equation 26 can then be extended to higher harmonics of effective polarizability as:

$$\alpha_{\text{eff},n} \propto \hat{F} \left[1 + \frac{f_0^{(B)}}{2} \sum_{j=1}^{\infty} \left(f_1^{(B)}\right)^{j-1} \beta^j \right] \quad (27)$$

This can be expanded then rearranged to the form:

$$\alpha_{\text{eff},n} \propto \delta(n) + \sum_{j=1}^{\infty} a_{j,n} \beta^j \quad (28)$$

$$a_{j,n} = \frac{\hat{F} \left[f_0^{(B)} \left(f_1^{(B)}\right)^{j-1} \right]}{2}$$

Here $\delta(n)$ represents the Dirac delta function, and $a_{j,n}$ represents the j^{th} Taylor coefficient. This series converges for $|\beta| < \sim 1$, which is generally true for weak molecular oscillators.

Truncating the series in equation 28 to a finite number of terms, J , means that an unknown β can be recovered from a known $\alpha_{\text{eff},n}$ by finding the roots of the resulting polynomial.

This typically leads to multiple solutions, as for a J^{th} -order complex polynomial there may be up to J unique roots. However, in practice, we find that these can usually be reduced to a single valid solution by rejecting solutions for which $|\beta| > \sim 1$ and optionally rejecting those for which $\text{Im}(\epsilon) < 0$.

4.4 Reflection coefficients

Accurate s-SNOM modelling requires calculation of both far-field (electrodynamic) and near-field (quasistatic) reflection coefficients. Multilayer FDM methods also require calculation of the effective quasistatic reflection coefficient for layered structures $\beta^{(M)}$.

Previous works have derived explicit equations for $\beta^{(M)}$ for particular numbers of layers, by repeated application of the method of image charges^{19,28}, but this is computationally challenging and requires a quickly expanding number of terms for each extra layer. Mester *et al.* proposed a way to generalize this to an arbitrary number of layers by recursively applying the equation for a 3-layer structure², but this fails for reflection coefficients close to zero (which can occur off-resonance in multilayer structures).

In snompy we instead adapt the TMM to calculate effective quasistatic reflection coefficients. This provides a computationally efficient method which works for arbitrary numbers of layers and has scope to be extended thanks to its relationship to the well-researched far-field TMM.

In this section we describe how electrodynamic and quasistatic reflection coefficients are calculated in snompy. We begin with a recap of the well-known electrodynamic TMM, then move on to describe how we adapted it to work for the quasistatic regime.

4.4.1 Electrodynamic

The TMM relates the field of electromagnetic waves on one side of a stack of interfaces to the other side.

In snompy we define that the interfaces are stacked, and that the fields propagate, in the z direction. Then for a layer A , we define field coefficients for forward and backwards travelling waves as R_A and L_A , and we define the z -component of the wavevector in the layer as $v_{z,A} = \sqrt{\epsilon_A v^2 - q^2}$ (where ϵ_A is the layer permittivity, v is the vacuum

wavenumber of the light, and q is the in-plane momentum).

Following the approach of Zhan *et al.* (2013)²² we define a transmission matrix, T_{AB} , which relates the fields immediately either side of a single interface between layers A and B as:

$$T_{AB} \begin{pmatrix} R_A \\ L_A \end{pmatrix} \equiv \begin{pmatrix} 1 + \rho_{AB} & 1 - \rho_{AB} \\ 1 - \rho_{AB} & 1 + \rho_{AB} \end{pmatrix} \begin{pmatrix} R_A \\ L_A \end{pmatrix} = \begin{pmatrix} R_B \\ L_B \end{pmatrix} \quad (29)$$

$$\rho_{AB} = \begin{cases} \frac{\epsilon_A v_{z,B}}{\epsilon_B v_{z,A}}, & \text{for p-polarization} \\ \frac{v_{z,B}}{v_{z,A}}, & \text{for s-polarization} \end{cases}$$

We also define a propagation matrix, P_A , which relates the fields at the start of layer A , with thickness t_A , to the fields at the end:

$$P_A \equiv \begin{pmatrix} e^{-iv_{z,A}t_A} & 0 \\ 0 & e^{iv_{z,A}t_A} \end{pmatrix} \quad (30)$$

Then for a sample formed of layers $0, 1, \dots, N - 1, N$, we can define a transfer matrix for the whole stack, via repeated matrix multiplication, as:

$$M \equiv T_{01} P_1 \dots P_{N-1} T_{(N-1)N} \quad (31)$$

Both s- and p-polarized reflection coefficients can then be obtained by

$$r = \frac{M[1, 0]}{M[0, 0]} \quad (32)$$

4.4.2 Quasistatic

In the quasistatic limit³², the z -component of wavevector becomes:

$$v_z = iq \quad (33)$$

Thanks to momentum conservation, q must be the same throughout the sample, meaning v_z is also constant and no longer depends on the permittivity of a particular layer. We can therefore replace

all $v_{z,A}$ and $v_{z,B}$ with iq to adapt the TMM to work for quasistatic reflection coefficients.

The transmission and propagation matrices then become:

$$T_{AB}^{(QS)} \equiv \begin{pmatrix} 1 + \frac{\epsilon_A}{\epsilon_B} & 1 - \frac{\epsilon_A}{\epsilon_B} \\ 1 - \frac{\epsilon_A}{\epsilon_B} & 1 + \frac{\epsilon_A}{\epsilon_B} \end{pmatrix} \quad (34)$$

$$P_A^{(QS)} \equiv \begin{pmatrix} e^{qt_A} & 0 \\ 0 & e^{-qt_A} \end{pmatrix},$$

Here a superscript (QS) refers to the quasistatic equivalent of an electrodynamic parameter. These can then be combined as for the electrodynamic case above, and the quasistatic reflection coefficient can be found from:

$$\beta^{(M)} = \frac{M^{(QS)}[1, 0]}{M^{(QS)}[0, 0]} \quad (35)$$

Note that the complex oscillation terms in the propagation matrix are replaced with exponentially decaying and growing* terms (representing evanescent, non-propagating fields).

4.5 Momentum integral discretization

In snompy, the computational efficiency of the multilayer FDM is optimized by careful treatment of semi-definite integrals with respect to in-plane momentum, q . See section 1.2 for a full description of these parameters.

For the Hauer multilayer method, these integrals are:

$$\varphi|_{z=0} = \int_0^\infty \beta^{(M)}(q) e^{-2z_0 q} dq, \quad \text{and} \quad (36)$$

$$E_z|_{z=0} = \int_0^\infty \beta^{(M)}(q) q e^{-2z_0 q} dq$$

*The e^{qt_A} term can be problematic as it can lead to numerical overflow for large values of qt_A . However we find that $\beta(q)$ typically converges for q values much smaller than this limit, so we can avoid this problem by simply clipping the output of e^{qt_A} to the maximum value for double-precision floating-point numbers without noticeably effecting the results.

For the charge average method this is:

$$\bar{\beta} = \frac{\int_0^\infty \beta^{(M)}(q) q e^{-2z_Q q} dq}{\int_0^\infty q e^{-2z_Q q} dq} \quad (37)$$

These are first rearranged and simplified, using the substitution $u = 2z_Q q$, to give:

$$\begin{aligned} \varphi|_{z=0} &= \frac{1}{2z_Q} \int_0^\infty \beta^{(M)} \left(\frac{u}{2z_Q} \right) e^{-u} du, \\ E_z|_{z=0} &= \frac{1}{4z_Q^2} \int_0^\infty \beta^{(M)} \left(\frac{u}{2z_Q} \right) u e^{-u} du, \quad \text{and} \quad (38) \\ \bar{\beta} &= \int_0^\infty \beta^{(M)} \left(\frac{u}{2z_Q} \right) u e^{-u} du \end{aligned}$$

We then make use of the Gauss-Laguerre approximation³³:

$$\int_0^\infty f(u) e^{-u} du \approx \sum_{m=1}^M w_m f(u_m) \quad (39)$$

Here u_m is the m^{th} root of the order- M Laguerre polynomial:

$$L_M(u) = \sum_{j=0}^M \binom{M}{j} \frac{(-1)^j}{j!} u^j \quad (40)$$

and w_m is a weight given by:

$$w_m = \frac{u_m}{((M+1)L_{M+1}(u_m))^2} \quad (41)$$

The integrals can therefore be approximated by the sums:

$$\begin{aligned} \varphi|_{z=0} &\approx \frac{1}{2z_Q} \sum_{m=1}^M \beta^{(M)} \left(\frac{u_m}{2z_Q} \right) w_m, \\ E_z|_{z=0} &\approx \frac{1}{4z_Q^2} \sum_{m=1}^M \beta^{(M)} \left(\frac{u_m}{2z_Q} \right) u_m w_m, \quad \text{and} \quad (42) \\ \bar{\beta} &\approx \sum_{m=1}^M \beta^{(M)} \left(\frac{u_m}{2z_Q} \right) u_m w_m \end{aligned}$$

The choice of M will affect the accuracy of the approximation, with higher values requiring more memory but leading to a more accurate evaluation. The weights and roots for a particular order, M , can be precomputed to speed up execution time.

4.6 Dielectric permittivity models

4.6.1 Hypothetical semiconductors

The hypothetical semiconducting samples shown in figure 1(b), are represented as bulk samples with a Drude function permittivity, ϵ_D , defined by:

$$\epsilon_D(\nu) = \epsilon_\infty - \frac{\nu_p^2}{\nu^2 + i\gamma\nu} \quad (43)$$

Here the parameter ϵ_∞ represents the high-frequency permittivity, ν_p is the plasma wavenumber, and γ is the damping rate

The specific parameters used to model the semiconductors are given below in table 5.

parameter	value
ϵ_∞	2
ν_p	10–10 cm ⁻¹
γ	$\frac{\nu_p}{3}$

Table 5: Hypothetical semiconductor permittivity parameters.

4.6.2 Poly(methyl methacrylate) (PMMA)

Figure 4(c) shows the simulated dielectric permittivity, ϵ_{PMMA} , used throughout this paper for PMMA close to its C=O bond. We chose the parameters of this model to produce the best agreement with the spectra shown in figures 4(a) and (b), while using the FDM parameters described by Mester *et al.* in the original reference from which the spectra were taken².

We represent the permittivity by an inhomogeneously broadened oscillator, defined by convolution of a Lorentzian oscillator, ϵ_L , with a Gaussian kernel, K_G , as:

$$\epsilon_{\text{PMMA}} = K_G(\nu) * \epsilon_L(\nu) \quad (44)$$

The Lorentzian oscillator is defined by:

$$\epsilon_L(\nu) = \epsilon_\infty + \frac{A_j}{\nu_j^2 - \nu^2 - i\gamma_j\nu} \quad (45)$$

Here the parameter ϵ_∞ represents the high-frequency permittivity, A_j is the oscillator amplitude, ν_j is the oscillator wavenumber, and γ_j is the oscillator width. The Gaussian kernel is defined as:

$$K_G(\nu) = \sqrt{\frac{\sigma_G}{\pi}} e^{-\sigma_G\nu^2} \quad (46)$$

Here σ_G is the width of the kernel, which defines degree of inhomogeneous broadening.

The specific parameters used to model PMMA are given below in table 6.

parameter	value
ϵ_∞	2.8
A_j	$4.6 \times 10^4 \text{ cm}^{-2}$
ν_j	1730 cm^{-1}
γ_j	2.1 cm^{-1}
σ_G	10.8 cm^{-1}

Table 6: PMMA permittivity parameters.

4.6.3 Graphene

To simulate the dielectric permittivity of graphene, ϵ_{gr} , we first model the frequency-, ω -, dependent optical conductivity using a simple Drude-type response* as:

$$\sigma_{gr} = \frac{Q_e^2 E_f}{\pi \hbar^2} \left(\frac{i}{\omega + \frac{i}{\tau}} \right) \quad (47)$$

Here Q_e is the electron charge, E_f is the Fermi energy of the graphene, \hbar is the reduced Planck constant, and τ is the scattering time for graphene

charge carriers³⁴.

We then convert this to a finite-thickness permittivity using:

$$\epsilon_{gr} = \epsilon_\infty + \frac{i\sigma_{gr}}{\epsilon_0\omega t_{gr}} \quad (48)$$

Here the parameter ϵ_∞ represents the high-frequency permittivity, ϵ_0 is the vacuum permittivity, and t_{gr} is the thickness of graphene.

The specific parameters used to model graphene are given below in table 7.

parameter	value
ϵ_∞	1
E_f	100 meV
τ	500 fs
t_{gr}	0.3 nm

Table 7: Graphene permittivity parameters.

References

1. Harris, C. R. *et al.* Array programming with NumPy. *Nature* **585**, 357–362. <http://dx.doi.org/10.1038/s41586-020-2649-2> (2020).
2. Mester, L., Govyadinov, A. A., Chen, S., Goikoetxea, M. & Hillenbrand, R. Subsurface chemical nanoidentification by nano-FTIR spectroscopy. *Nature Communications* **11**. <http://dx.doi.org/10.1038/s41467-020-17034-6> (2020).
3. Hauer, B., Engelhardt, A. P. & Taubner, T. Quasi-analytical model for scattering infrared near-field microscopy on layered systems. *Optics Express* **20**, 13173. <http://dx.doi.org/10.1364/oe.20.013173> (2012).

*There are more accurate models of graphene's optical conductivity, such as the local and non-local random phase approximation³⁴, but the Drude response is sufficient for the simple demonstration here.

4. Chen, J. *et al.* Plasmonic Nickel Nanoantennas. *Small* **7**, 2341–2347. <http://dx.doi.org/10.1002/smll.201100640> (2011).
5. Hu, D. *et al.* Probing optical anisotropy of nanometer-thin van der waals microcrystals by near-field imaging. *Nature Communications* **8**. <http://dx.doi.org/10.1038/s41467-017-01580-7> (2017).
6. Fei, Z. *et al.* Gate-tuning of graphene plasmons revealed by infrared nano-imaging. *Nature* **487**, 82–85. <http://dx.doi.org/10.1038/nature11253> (2012).
7. Vincent, T. *et al.* Strongly Absorbing Nanoscale Infrared Domains within Strained Bubbles at hBN-Graphene Interfaces. *ACS Applied Materials & Interfaces* **12**, 57638–57648. <http://dx.doi.org/10.1021/acscami.0c19334> (2020).
8. Greaves, G. E., Kiryushko, D., Auner, H. W., Porter, A. E. & Phillips, C. C. Label-free nanoscale mapping of intracellular organelle chemistry. *Communications Biology* **6**. <http://dx.doi.org/10.1038/s42003-023-04943-7> (2023).
9. Kaltenecker, K. J., Gözl, T., Bau, E. & Keilmann, F. Infrared-spectroscopic, dynamic near-field microscopy of living cells and nanoparticles in water. *Scientific Reports* **11**. <http://dx.doi.org/10.1038/s41598-021-01425-w> (2021).
10. Dai, S. *et al.* Graphene on hexagonal boron nitride as a tunable hyperbolic metamaterial. *Nature Nanotechnology* **10**, 682–686. <http://dx.doi.org/10.1038/nnano.2015.131> (2015).
11. Chen, L. *et al.* Near-field imaging of the multi-resonant mode induced broadband tunable metamaterial absorber. *RSC Advances* **10**, 5146–5151. <http://dx.doi.org/10.1039/c9ra10233g> (2020).
12. Sunku, S. S. *et al.* Photonic crystals for nano-light in moiré graphene superlattices. *Science* **362**, 1153–1156. <http://dx.doi.org/10.1126/science.aau5144> (2018).
13. Mester, L., Govyadinov, A. A. & Hillenbrand, R. High-fidelity nano-FTIR spectroscopy by on-pixel normalization of signal harmonics. *Nanophotonics* **11**, 377–390. <http://dx.doi.org/10.1515/nanoph-2021-0565> (2021).
14. Mooshammer, F. *et al.* Nanoscale Near-Field Tomography of Surface States on $(\text{Bi}_{0.5}\text{Sb}_{0.5})_2\text{Te}_3$. *Nano Letters* **18**, 7515–7523. <http://dx.doi.org/10.1021/acs.nanolett.8b03008> (2018).
15. Plankl, M. *et al.* Subcycle contact-free nanoscopy of ultrafast interlayer transport in atomically thin heterostructures. *Nature Photonics* **15**, 594–600. <http://dx.doi.org/10.1038/s41566-021-00813-y> (2021).
16. Chen, S. *et al.* Real-space nanoimaging of THz polaritons in the topological insulator Bi_2Se_3 . *Nature Communications* **13**. <http://dx.doi.org/10.1038/s41467-022-28791-x> (2022).
17. Keilmann, F. & Hillenbrand, R. Near-field microscopy by elastic light scattering from a tip. *Philosophical Transactions of the Royal Society of London. Series A: Mathematical, Physical and Engineering Sciences* **362**, 787–805. <http://dx.doi.org/10.1098/rsta.2003.1347> (2004).
18. Cvitkovic, A., Ocelić, N. & Hillenbrand, R. Analytical model for quantitative prediction of material contrasts in scattering-type near-field optical microscopy. *Optics Express* **15**, 8550. <http://dx.doi.org/10.1364/oe.15.008550> (2007).
19. Hauer, B., Engelhardt, A. P. & Taubner, T. Quasi-analytical model for scattering infrared near-field microscopy on layered systems. *Optics Express* **20**, 13173. <http://dx.doi.org/10.1364/oe.20.013173> (2012).
20. Mester, L. *Substrate-enhanced and subsurface infrared near-field spectroscopy of organic layers* PhD thesis (CIC nanoGUNE, 2020). <https://www.nanogune.eu/en/publications/phd-theses/>.

21. McLeod, A. S. *et al.* Model for quantitative tip-enhanced spectroscopy and the extraction of nanoscale-resolved optical constants. *Physical Review B* **90**. <http://dx.doi.org/10.1103/physrevb.90.085136> (2014).
22. Zhan, T., Shi, X., Dai, Y., Liu, X. & Zi, J. Transfer matrix method for optics in graphene layers. *Journal of Physics: Condensed Matter* **25**, 215301. <http://dx.doi.org/10.1088/0953-8984/25/21/215301> (2013).
23. Aizpurua, J., Taubner, T., García de Abajo, F. J., Brehm, M. & Hillenbrand, R. Substrate-enhanced infrared near-field spectroscopy. *Optics Express* **16**, 1529. <http://dx.doi.org/10.1364/oe.16.001529> (2008).
24. Govyadinov, A. A., Amenabar, I., Huth, F., Carney, P. S. & Hillenbrand, R. Quantitative Measurement of Local Infrared Absorption and Dielectric Function with Tip-Enhanced Near-Field Microscopy. *The Journal of Physical Chemistry Letters* **4**, 1526–1531. <http://dx.doi.org/10.1021/jz400453r> (2013).
25. Govyadinov, A. A. *et al.* Recovery of Permittivity and Depth from Near-Field Data as a Step toward Infrared Nanotomography. *ACS Nano* **8**, 6911–6921. <http://dx.doi.org/10.1021/nm5016314> (2014).
26. Barnett, J. *et al.* Phonon-Enhanced Near-Field Spectroscopy to Extract the Local Electronic Properties of Buried 2D Electron Systems in Oxide Heterostructures. *Advanced Functional Materials* **30**. <http://dx.doi.org/10.1002/adfm.202004767> (2020).
27. Ocelić, N. *Quantitative Near-Field Phonon-Polariton Spectroscopy* PhD thesis (Technische Universität München, 2007). <https://mediatum.ub.tum.de/624573>.
28. Lupo, C. *et al.* *Quantitative infrared near-field imaging of suspended topological insulator nanostructures* 2021. arXiv: 2112.10104 [cond-mat.mes-hall].
29. Virtanen, P. *et al.* SciPy 1.0: fundamental algorithms for scientific computing in Python. *Nature Methods* **17**, 261–272. <http://dx.doi.org/10.1038/s41592-019-0686-2> (2020).
30. Chen, X. *et al.* Rapid simulations of hyperspectral near-field images of three-dimensional heterogeneous surfaces. *Optics Express* **29**, 39648. <http://dx.doi.org/10.1364/oe.440821> (2021).
31. Chen, X. *et al.* Rapid simulations of hyperspectral near-field images of three-dimensional heterogeneous surfaces - part II. *Optics Express* **30**, 11228. <http://dx.doi.org/10.1364/oe.452949> (2022).
32. Skaar, J. Fresnel's equations in statics and quasistatics. *European Journal of Physics* **40**, 045201. <http://dx.doi.org/10.1088/1361-6404/ab166b> (2019).
33. Ehrich, S. On stratified extensions of Gauss-Laguerre and Gauss-Hermite quadrature formulas. *Journal of Computational and Applied Mathematics* **140**, 291–299. [http://dx.doi.org/10.1016/s0377-0427\(01\)00407-1](http://dx.doi.org/10.1016/s0377-0427(01)00407-1) (2002).
34. Koppens, F. H. L., Chang, D. E. & García de Abajo, F. J. Graphene Plasmonics: A Platform for Strong Light-Matter Interactions. *Nano Letters* **11**, 3370–3377. <http://dx.doi.org/10.1021/nl201771h> (2011).

Acknowledgements

We thank Iris Niehues, Martin Schnell and Edoardo Vicentini from CIC nanoGUNE, as well as Alexander Govyadinov from Attocube Systems AG, for their helpful comments during the preparation of snompy and this manuscript.

We would like to thank UKRI and EPSRC for research funding via projects MR/T022140/1, EP/S037438/1, and the NAME programme grant (EP/V001914/1), as well as the Henry Royce Institute for access to the CUSTOM facility at the University of Manchester (EP/T01914X/1). We also acknowledge the support of the UK government Department for Science, Innovation and Technology through the UK National Quantum Technologies Programme.

Glossary

- A_j Lorentzian oscillator strength. 21
- A initial layer. 18, 19, 24
- B subsequent layer. 19, 24
- E_f Fermi energy. 21
- E_s scattered electric field strength. 4
- E_z z-component of electric field. 7, 19, 20
- E_{in} incident electric field strength. 4–6
- G arbitrary function. 17
- J Maximum degree for a truncated Taylor expansion. 18
- K_G Gaussian kernel. 20, 21
- L backwards travelling wave. 18, 19
- P_A layer propagation matrix. 19
- Q_e electron charge. 21
- Q charge. 6, 7, 16, 19, 20, 24, 25
- R forward travelling wave. 18, 19
- T_{AB} interface transfer matrix. 19
- A_{tip} AFM tapping amplitude. 9, 10, 16, 17
- L_{tip} FDM ellipsoid semi-major axis length. 6, 7, 9, 10, 16, 17
- z_{tip} AFM tip-sample separation. 3, 6–9, 16, 17
- r_{tip} AFM tip apex radius of curvature. 6–10, 16, 17
- $\alpha_{eff,n}$ n^{th} -harmonic demodulated effective polarizability. 5, 12, 15, 17, 18, 25
- α_{eff} effective polarizability. 4, 6, 7, 15, 18, 24, 25
- α_{tip} polarizability of a dielectric sphere representing the tip. 7, 8, 16
- β quasistatic reflection coefficient. 4, 6, 7, 12, 14, 17–20, 24, 25
- η s-SNOM contrast. 5, 12–15, 17, 24
- γ carrier damping frequency. 20, 21, 24
- Q_0 charge 0. 6, 7, 16, 24, 25
- Q_1 charge 1. 6, 7, 16, 24, 25
- Q_j arbitrary charge. 6, 7, 24, 25
- Q_a single representative charge. 7, 16, 25
- $\beta^{(M)}$ multilayer effective quasistatic reflection coefficient. 7, 18–20
- $\beta_{Q'_0}$ effective reflection coefficient for charge Q_j . 7
- $\beta_{Q'_1}$ effective reflection coefficient for charge Q_j . 7
- $\beta_{Q'_j}$ effective reflection coefficient for charge Q_j . 7
- $d_{Q'_j}$ depth of an image of charge Q_j . 7
- ϵ_0 vacuum permittivity. 21
- ϵ_D Drude function permittivity. 20
- ϵ_L Lorentzian oscillator permittivity. 20, 21
- ϵ_∞ high-frequency permittivity. 20, 21
- ϵ_{env} environment permittivity. 6
- ϵ_{sub} substrate permittivity. 6
- ϵ_{tip} tip permittivity. 8, 16, 17
- η_n n^{th} -harmonic demodulated s-SNOM contrast. 5, 12, 15, 17
- γ_j oscillator carrier damping frequency. 21
- $f^{(B)}$ bulk FDM geometry function. 6, 7, 18
- $f^{(M)}$ multilayer FDM geometry function. 6, 7
- $f^{(P)}$ point dipole model FDM geometry function. 7, 8
- ν_j Lorentzian oscillator wavenumber. 21
- ν_p plasma wavenumber. 2, 3, 20
- ϕ_n n^{th} -harmonic demodulated s-SNOM phase. 3, 5, 11–13, 17
- r_p p-polarized Fresnel reflection coefficient. 3–5

- σ_n n^{th} -harmonic demodulated near-field scattering constant. 5
- s_n n^{th} -harmonic demodulated s-SNOM amplitude. 3, 5, 11–13, 17
- z_{Q_0} height of a charge Q_0 . 6, 16
- z_{Q_1} height of a charge Q_1 . 6, 16
- z_{Q_a} height of a charge Q_a . 7, 16
- z_{Q_j} height of a charge Q_j . 6, 7
- z_Q height of a generic charge Q . 19, 20
- \hbar reduced Planck constant. 21
- δ dirac delta operator. 18
- $\hat{\Gamma}$ tip demodulation operator. 17, 18
- (B) symbol denoting bulk sample. 6, 7, 18, 24
- (M) symbol denoting multilayer sample. 6, 7, 18–20, 24
- (P) symbol denoting point dipole model. 7, 8, 24
- (obs) symbol denoting observed value. 12
- (ref) symbol denoting reference sample for normalization. 5
- (test) symbol denoting test value. 12
- ν vacuum wavenumber. 2, 3, 18–21, 24
- ω angular frequency. 21
- $\bar{\beta}$ Charge-average-method definition of the effective quasistatic reflection coefficient. 7, 20
- ϕ s-SNOM phase. 3, 5, 7, 8, 11–14, 17, 24
- σ_G Gaussian standard deviation. 21
- σ_{gr} sheet conductivity of graphene. 21
- σ near-field scattering constant. 4, 5, 25
- τ carrier relaxation time. 21
- ε relative permittivity. 2–4, 6, 8–14, 16–21, 24
- φ electric potential. 7, 19, 20
- $a_{j,n}$ j^{th} Taylor coefficient of n^{th} -harmonic demodulated effective polarizability. 18
- d depth below the surface. 7, 24
- e Euler's number. 5, 6, 17, 19, 21
- f FDM geometry function. 6–8, 18, 24
- g FDM g factor. 6, 7, 16, 17
- i imaginary unit. 5, 6, 17, 19–21
- j index variable. 6, 7, 18, 20, 21, 24, 25
- m index variable. 20
- n harmonic. 2, 3, 5, 11–13, 15–18, 24, 25
- p_0 FDM dipole 0. 6
- p_1 FDM dipole 1. 6
- q in-plane wavevector component. 3, 7, 18–20
- r Fresnel reflection coefficient. 3–5, 24
- s s-SNOM amplitude. 3, 5, 8, 11–14, 17, 25
- t layer thickness. 2, 19, 21
- u integration substitution variable. 20
- z spatial dimension perpendicular to sample plane. 3, 6–9, 16–20, 24, 25

Acronyms

- AFM** atomic force microscopy. 2–9, 16, 17, 24
- FDM** finite dipole model. 1–15, 17–20, 24, 25
- FTIR** Fourier transform infrared. 1–4, 8, 9, 12
- IR** infrared. 2, 5, 8
- LRM** lightning rod model. 2, 15
- PDM** point dipole model. 1–4, 7, 9, 11, 15, 17
- PMMA** poly(methyl methacrylate). 2, 3, 8–11, 20, 21
- PS** poly(styrene). 2, 3

s-SNOM scattering-type scanning near-field optical microscopy. 1-4, 7-9, 11-15, 17, 18, 24, 25

TMM transfer matrix method. 2-4, 18, 19